Int. J. Electrochem. Sci., 17 **(2022)** Article Number: 221163, doi: 10.20964/2022.11.79

International Journal of
ELECTROCHEMICAL
SCIENCE
www.electrochemsci.org

Microbial Corrosion of L360N Steel in Simulated Flowback Water of Shale Gas Field

Yanran Wang[*], *Yongfan Tang*, *Huali Yu*

Research Institute of Natural Gas Technology, PetroChina Southwest Oil & Gasfield Company, Chengdu, Sichuan, China.
[*]E-mail: 2858782013@qq.com

Received: 6 July 2022 / *Accepted:* 6 October 2022 / *Published:* 20 October 2022

A large amount of flowback water (FBW) is generated during the shale gas exploitation. Since FBW contains a large number of corrosive ions and bacteria, pipeline steel often suffers from serious corrosion, affecting its safe operation. In this paper, the corrosion of L360N steel in simulated FBW solution containing SRB and without SRB was studied using electrochemical measurement, weight-loss tests, Raman spectra, and scanning electron microscope (SEM). The results show that the corrosion morphology of L360N steel is pitting corrosion, and the corrosion rate of coupon when adding SRB is about 5 times of that without SRB. The corrosive anions in synergy with SRB enhanced the corrosion of L360N steel.

Keywords: Shale gas; Sulfate-reducing bacteria; Electrochemical reaction; Corrosion product; Biofilm

1. INTRODUCTION

In recent years, with the increasing share of natural gas in fossil energy consumption, China has begun the exploration for shale gas [1]. It is reported that the annual output of shale gas has reached 10^{10} m^3 in the southern Sichuan Basin [2]. The Shale Gas field in Sichuan Basin is one of the most typical gas fields with daily gas production over 3×10^7 m^3.

The development and utilization of shale gas is bound to play a decisive role in Chinese future energy development [3, 4]. According to the geological conditions, industrial practices and the current limitations of full-scale development of shale gas in Sichuan Basin, a new concept of "volume development (VD)" has been proposed. Volumetric fracturing technology is commonly used in shale gas production. The single well fracturing fluid dosage is 4×10^4–5×10^4 m^3 and the proppant (quartz sand ceramsite) dosage is 2.5×10^3–3.0×10^3 t. In the process of shale gas drainage and production, after fracturing is completed, flowback water (FBW) causes varying degrees of corrosion to the surface

drainage process and surface gathering and transportation system, which may result in equipment and pipeline failures and affect the safe operation of the production system [5, 6]. Corrosion has always been one of the most prominent issues affecting the safety of shale gas fields, and the equipment failure caused by corrosion accounts for 25%. Especially, the water and corrosive medium in the pipeline exert a vital influence on the corrosion rate [7].

In addition, the analysis found that FBW contained Cl^- and abundant bacteria [8]. However, microbiologically influenced corrosion (MIC) is one of the major issues in oil and shale gas field exploitation [9-12].

At the early stage of shale gas production, there are few bacteria in FBW, but with the recycling of FBW, abundant organic carbon sources have been accumulated in FBW. These organic carbon sources provide sufficient nutrients for the bacteria reproduction. Especially in organic carbon-rich FBW, the number of bacteria is close to 10^{10} cells mL^{-1} [13]. A large number of studies have been carried out on the MIC mechanism of pipeline steel [14-18].

In particular, sulfate reducing bacteria (SRB) was found as early as 1926 and considered to be one of the most corrosive bacteria to pipeline steel [19-21]. For decades, SRB has been widely studied as an important MIC pathogen. The mechanism of SRB corrosion of metal is mainly explained by cathode depolarization theory [22], concentration difference battery theory [23], metabolite theory [24, 25] and anode acceleration theory [26]. Pankhania proposed that the cathodic process of metal corrosion is a hydrogen reduction process without oxygen or at very low oxygen [27]. That is, hydrogen atoms will form hydrogen molecules, which requires very high activation energy, so the thermodynamic process is difficult. But SRB can produce hydrogenase, which can use the hydrogen atoms adsorbed on the surface of the cathode to reduce sulfate ions and obtain survival energy from it. Hydrogen molecules are removed during the cathode process, leading to cathode depolarization and accelerating metal corrosion. Xu described the mechanistic mode of MIC caused by SRB sulfate reduction based on the biocatalytic cathodic sulfate reduction (BCSR) theory [28]. Jia et al. proposed that extracellular electron transfer dominated the SRB corrosion process [29]. Yan et al. showed that SRB could regulate the respiratory metabolism in the SO_4^{2-} deficient environment, and use Fe(III), Mn(IV), and H_2 as terminal electron acceptors for extracellular respiration to maintain survival metabolism and promote the corrosion process of carbon steel [30, 31]. Furthermore, extracellular polymer substance (EPS) can accelerate the localized corrosion of steel by enhancing the anode reaction [32].

In addition, other microorganisms in the solution can also cause pipeline corrosion failure. A recent study revealed that there was a severe MIC problem in Pinedale shale gas field, and a large number of bacteria were detected in the FBW [33]. Wang and Li et al. studied the effects of *Bacillus cereus* and *Brevibacterium halotolerans* on X80 pipeline steel in the presence of MIC [34, 35]. Studies have shown that both types of bacteria can accelerate the pitting corrosion of steel. It has also been reported that iron-oxidizing bacteria (IOB) in oilfield water leads to the failure of metal materials [36, 37].

However, there are few studies on SRB for FBW. Studying the corrosion of FBW containing SRB shale gas can effectively develop the corresponding MIC anticorrosion technology.

In this paper, the effect of the corrosion of L360N steel in sterile and inoculated FBW was studied through electrochemical measurements, X-ray photoelectron spectroscopy (XPS), scanning electron

microscope (SEM), energy dispersive spectrometer (EDS) and Confocal laser scanning microscopy (CLSM).

2. EXPERIMENT

2.1 Metal samples preparation

L360N is a commonly used pipeline in oil and gas field pipelines in Changning area, among which the L360N pipe steel is mostly used for gathering pipelines, water injection pipelines and sewage pipelines. Therefore, the test material in this paper is taken from the pipeline steel of Changning shale gas field in Sichuan. L360N steel with chemical composition (wt%) of C 0.2, Si 0.35, Mn 1.42, S 0.019, P 0.02 was used as corrosion coupon, and Fe was balanced. The coupon was sealed by epoxy resins, and only one end face (10 mm× 10 mm) was exposed. The working surface of the coupon was subsequently ground with silicon carbide metallurgical paper (from 120 grit to 600 grit), cleaned in distilled water, washed with anhydrous ethanol, and finally dried under nitrogen gas.

2.2 High throughput sequencing of 16S rRNA gene amplicon

The genomic DNA of the sample was extracted by CTAB or SDS method, and then the purity and concentration of the DNA were detected by agarose gel electrophoresis. Appropriate amount of sample DNA was put into a centrifuge tube, and diluted to 1ng/μl with sterile water.

Using the diluted genomic DNA as a template, according to the selection of the sequencing region, specific primers with Barcode, Phusion® High-Fidelity PCR Master Mix with GC Buffer from New England Biolabs, and high-efficiency and high-fidelity enzymes were used for PCR to ensure the amplification efficiency and accuracy. Primer corresponding region:16S V4 region primers (515F and 806R): identification of bacterial diversity; 18S V4 region primers (528F and 706R): identification of eukaryotic microbial diversity; ITS1 region primers (ITS5-1737F and ITS2-2043R): identification of fungal diversity; In addition, the amplified regions include: 16S V3-V4/16S V4-V5/16SV5-V7; Archaeal 16S V4-V5/Archaeal 16S V8; 18S V9 and ITS2 regions.

The TruSeq® DNA PCR-Free Sample Preparation Kit was used for library construction. The constructed library was quantified by Qubit and Q-PCR. After the library was qualified, NovaSeq6000 was used for on-machine sequencing. The strain was identified preliminarily as Desulfovibrio desulfuricans (DQ092636) with similarity of 97%.

2.3 SRB culture and Test solution

SRB strains were obtained from the fracturing FBW of the shale gas field in Sichuan Basin. The ATCC-1249 medium used in this study contained 2.0g/L $MgSO_4$， 5.0 g/L Sodium citrate, 1.0 g/L $CaSO_4$, 1.0 g/L NH_4Cl, 0.5 g/L K_2HPO_4, 3.5 g/L Sodium lactate, 1.0 g/L Yeast extract, and 5ml 5%(w/w) $Fe(NH_4)_2(SO_4)_2$ g/L. After inoculation, the initial cell concentration was approximately 10^6 cells/mL and

the pH of the medium was adjusted to 7.5 by 1mol/L NaOH. The culture medium was sparged with the high purity N_2 gas for 2 h to remove the dissolved O_2. Before use, the culture medium was autoclaved at 121℃ for 20 min and stored at 4℃. SRB number was determined by the three-tube multiple most probable number (MPN) method according to the ASTM Standard D4412-84.

The test solution is the simulated FBW of Changning shale gas field, Sichuan. The chemical composition of the simulated FBW in the shale gas field is shown in Table 1. Before the test, the high purity N_2 gas containing 5% CO_2 was purged to the simulated FBW solution for 2 h to reach the anaerobic state. This test used ATCC-1249 medium (inoculated) to accumulate simulated FBW solution with an accumulation of 5.0 vol.% SRB . In addition, 5 vol.% sterilized medium was added to the simulated FBW solution for sterile control, so that the biotic and abiotic environments were equivalent (Sterile). All experiments were conducted in a sterile glove box filled with N_2.

Table 1. Chemical composition of the simulated FBW in the shale gas field

Chemical Composition	Cl^-	SO_4^{2-}	Ca^{2+}	Mg^{2+}	HCO_3^-	Na^++K^+
Ion concentration (mg/L)	25000	300	800	100	500	Bal.

2.4 Weight-loss measurement

Weight loss was calculated according to the NACE protocols (TM0169-2000) to determine the corrosion rate of the L360N steel coupons exposed to the simulated FBW under two conditions (Inoculated FBW and Sterile FBW). Three weight-loss coupons were machined to the size of 10 mm × 10 mm × 3 mm and vernier caliper (accuracy =± 0.1mm) was used to determine the size of each coupon. Before the experiment, the surface was polished with 120, 240, 400 and 600 grit SiC papers, washed with acetone and then dried with dryer. The weight loss measurement was started by immersing the coupons in the inoculated FBW and the sterile FBW for 21 days. The corrosion products were cleaned by a rust removal solution ASTM G1-03 (500 ml HCl, 500 ml H_2O and 3.5 g $(CH_2)_6N_4$).The initial and final weight of the dried coupons were determined by analytical equilibrium method. The corrosion rate of weight-loss coupons can be obtained by the following equation:

$$V_{corr} = \frac{534.57\times(W_0-W_1)}{\rho\times S\times t} \quad (1)$$

Where V_{corr} is the corrosion rate (mpy); W_0 is the initial weight of the coupon; W_1 is the weight of the coupon after the corrosion product is removed; ρ is the L360N steel density (g/cm^3); S is the surface of L360N steel coupon (cm^2); t is the immersion time (h).

2.5 Electrochemical measurements

All electrochemical measurements were conducted with Gamry 600+ for electrochemical testing. To maintain the homogeneity of the test solution, a five-link electrolytic cell was used in the test device,

as shown in Figure 1. All the measurements were carried out in a three-electrode electrochemical cell, with L360N steel as the working electrode, platinum plate as the auxiliary electrode and reference electrode as saturated calomel electrode (SCE). The LPR curves were measured at the scanning rate of 0.166 mV/s, and the scanning range was from −20.0 mV to +20.0 mV (vs open circuit potential, OCP). EIS test excitation signal was 10 mV sine wave, and the test frequency range was 10^{-2}~10^{5} Hz. The EIS data were fitted by ZSimpWin software. All electrochemical tests were performed at 30 ± 2 ℃ and repeated three times. The scanning range of Tafel polarization measurements was from -300.0 mV vs OCP to 300.0 mV vs OCP, and the scanning rate was 0.5 mV/s.

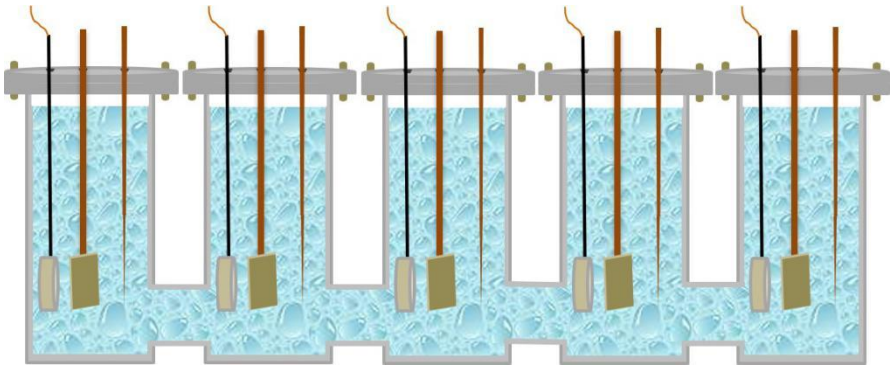

Figure 1. Schematic diagram of the experimental set-up for studies of L360N steel

2.6 Surface and corrosion products characterization

After the immersion test, all the coupons were taken out. The inoculated coupons used for biofilm morphology observation were treated with microbial fixation and dehydration: The bacteria were solidified in phosphate-buffered saline (PBS) solution containing 4% (*w/w*) glutaraldehyde solution ($C_5H_8O_2$) for 2h, washed twice with PBS and deionized water (5 min each time), and then dehydrated with 50%, 75%, 95% and 100% (*w/w*) alcohol for 10 min each time, and then dried with high purity N_2. SEM (XL30-FEG, Holland) was used to analyze the composition of corrosion products by energy spectrum (EDS) and the surface corrosion of the coupon was observed.

Surface chemical composition of biofilm was analyzed by Raman spectrometer (SO-TN04, Japan). XPS (ESCALAB 250, USA) was used to analyze the chemical states of iron and sulfur compounds. The high definition S orbital spectrum at 50 eV was obtained by standard C, and curve fitting was performed using XPS PEAK software (Version 4.1). The Confocal Laser Scanning Microscope (CLSM) (LSM 900, GER) with eyepiece magnification of x10 and objective magnification of x20 was used to count and measure the maximum pitting depth of the coupons after removal of corrosion products.

3. RESULTS AND DISCUSSION

3.1 Growth characteristics of planktonic SRB cell

The growth curve of SRB over time is shown in Figure 2. The results showed that the number of suspended bacteria in the simulated FBW inoculated with SRB increased first and then decreased with the extension of inoculation time. In the simulated FBW containing 5% medium, the growth of SRB was suitable for the first three days, so the number of SRB bacteria increased exponentially at the initial stage, and reached the maximum at the second day, about 1.4×10^9 CFU/mL. Later, due to nutrient depletion, the number of bacteria gradually decreased to about 1.5×10^7 CFU/mL by the 21st days .

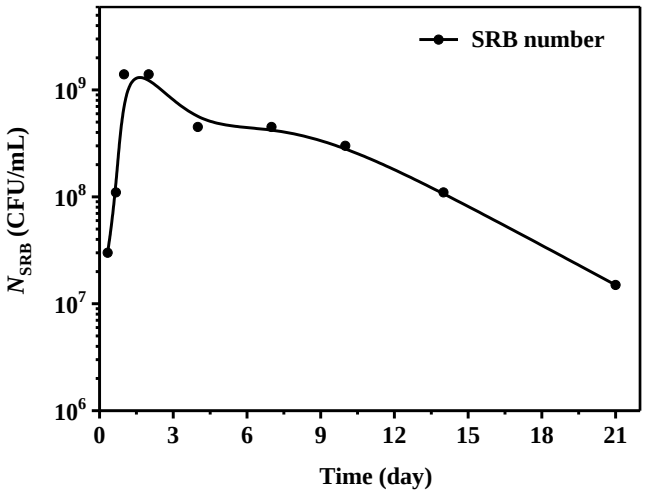

Figure 2. Growth curve of SRB in the simulated FBW by MPN method at 25℃

3.2 Weight-loss analysis

The corrosion rate of L360N steel obtained from the weight-loss data under FBW conditions is shown in Figure 3. In the Inoculated FBW and Sterile FBW, the corrosion rates are 0.2457 ± 0.0358 mpy and 1.0627 ± 0.05916 mpy respectively.

In the Inoculated FBW, the corrosion rate of the coupon is 5 times higher than that of the Sterile FBW.The results mentioned above indicate that the SRB enhances the corrosion of L360N steel in FBW. Xu and Liu [28, 38] found that the SRB biofilm with longer pre-culture time accelerated the corrosion rate of the steel. Wu et al.[17] also reported that SRB activities enhanced steel corrosion, indicating that the semi-conductive iron sulfide corrosion products can transfer electrons from Fe^0 to SRB biofilm.

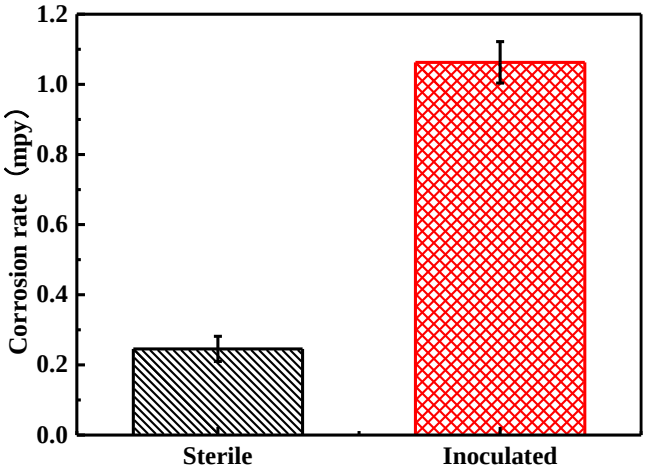

Figure 3. The corrosion rates of L360N steel after immersion by ASTM G1-03 at 25℃ for 21 days

3.3 LPR measurements

In electrochemical measurement, the LPR is considered as an available electrochemical method to measure the corrosion rate, which is inversely proportional to the R_p value [39]. The change of polarization resistance in the simulated FBW under two conditions is shown in Figure 4. On the 3rd, 7th, 14th and 21st day, the R_p value in the inoculated FBW was lower than that in the sterile FBW, indicating that the corrosivity of the simulated solution with SRB was higher than that without SRB, which also indicated that SRB was involved in the corrosion process and accelerated the corrosion of L360N steel.

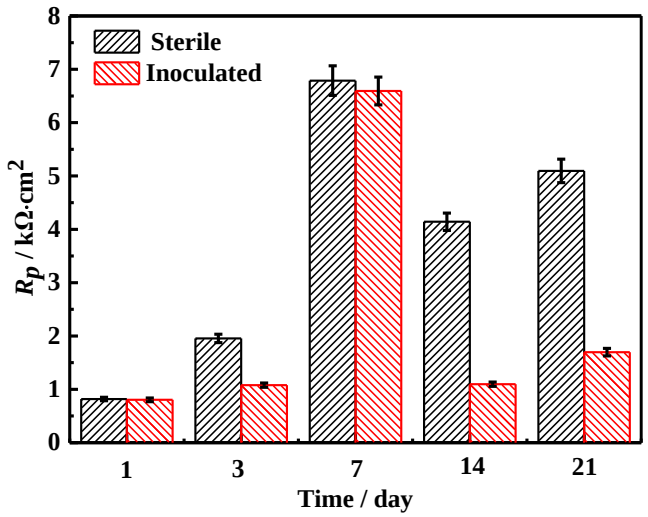

Figure 4. The change of R_p value for 1 d, 3 d, 7 d, 14 d and 21 d respectively in the sterile and inoculated FBW

3.4 EIS results analysis

Equivalent electrical circuits R_s (Q_{dl} R_{ct}) was used to fit EIS-Nyquist diagrams of the steel in the sterile and inoculated FBW, as shown in Figure 5 (a). Where R_s, Y_{dl} and R_{ct} represent the solution resistance, bilayer capacitance and the charge transfer resistance respectively. The impedance of the

constant phase element (CPE) is employed and expressed by the equation [40].

$$Z_{CPE} = Y_0^{-1}(j\omega)^{-n} \quad (2)$$

Where Y_0 is the parameter of approximate capacitance and n is the CPE index, j is the imaginary number and ω is the angular frequency.

The EIS-Nyquist diagrams of the sterile and FBW after 1, 3, 7, 14, and 21 days are presented in Figure 5 (b-f). Figure 5. (b) - (f) show that the capacitive arc radius of the inoculated FBW is smaller than that of sterile FBW.

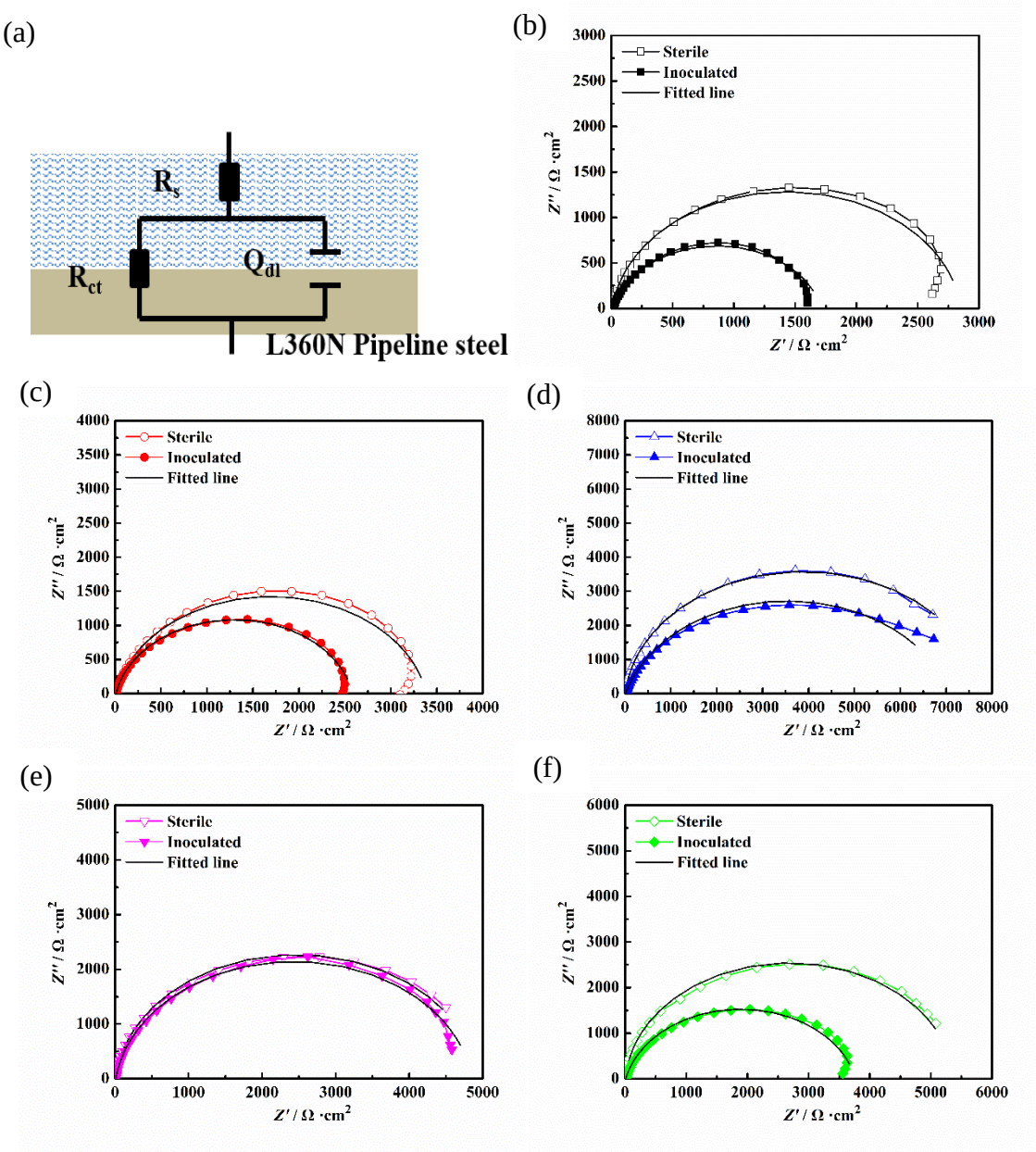

Figure 5. Nyquist plots of L360N steel in the sterile and inoculated FBW (a) Equivalent Circuit Model, (b) 1d, (c) 3d, (d) 7d, (e)14d, (f) 21d, test excitation signal 10 mV sine wave , frequency range 10^{-2}~10^5 Hz

Table 2. Fitted EIS parameters of L360N steel coupons for 1 d, 3 d, 7 d, 14 d and 21 d respectively in the sterile and inoculated FBW

Time (d)	R_s ($\Omega \cdot cm^2$)		Y_{dl} ($S \cdot s^n \cdot cm^{-2}$)		n_{dl}		R_{ct} ($\Omega \cdot cm^2$)	
	sterile	inoculated	sterile	inoculated	sterile	inoculated	sterile	inoculated
1	9.425	16.64	0.0004283	0.0003027	0.9346	0.8662	2844	1695
3	8.409	12.32	0.0002079	0.0003334	0.8909	0.8925	3381	2570
7	9.699	11.73	0.0004094	0.0002949	0.9496	0.8349	7748	7052
14	8.318	11.82	0.0006595	0.0002879	0.9473	0.9202	4925	4801
21	10.19	11.81	0.0004753	0.00023	0.9652	0.8686	5371	3756

ZsimpWin software was used to analyze the impedance of the corrosion product film of L360N steel, and the fitting results of EIS-Nyquist diagrams are shown in Table 2. It was also evident from Table 2 that the R_{ct} value obtained by the fitting of the sterile FBW was significantly greater than that of the inoculated FBW. The charge transfer resistance R_{ct} is inversely proportional to the corrosion rate [41, 42]. The above EIS data showed that the corrosion resistance of L360N steel decreased due to SRB.

3.5 Potentiodynamic polarization curves measurement

Figure 6 shows the polarization curves of L360N steel coupons in the sterile and inoculated FBW after 1, 3, 7, 14, 21 days. During the experiment, in sterile FBW, all the coupons were dissolved with anodic activity, and the corrosion currents were significantly different. Table 3 shows the corrosion parameters of L360N steel coupons, including the corrosion current density (i_{corr}), the corrosion potential (E_{corr}), the cathode Tafel slope (βc) and the anode Tafel slope (βa). At 21 d, the values of i_{corr} of this experiment were 0.944 and 7.37 μA cm^{-2} for sterile and inoculated coupons.

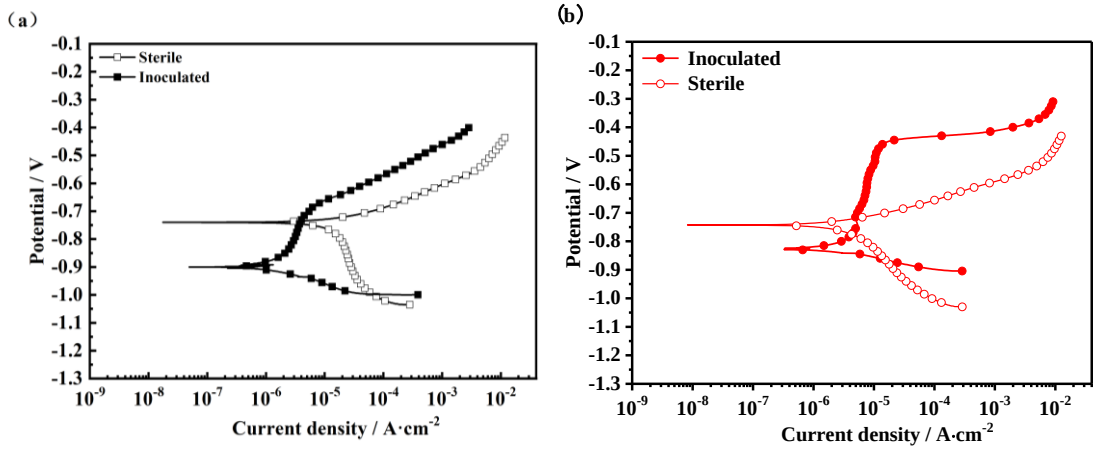

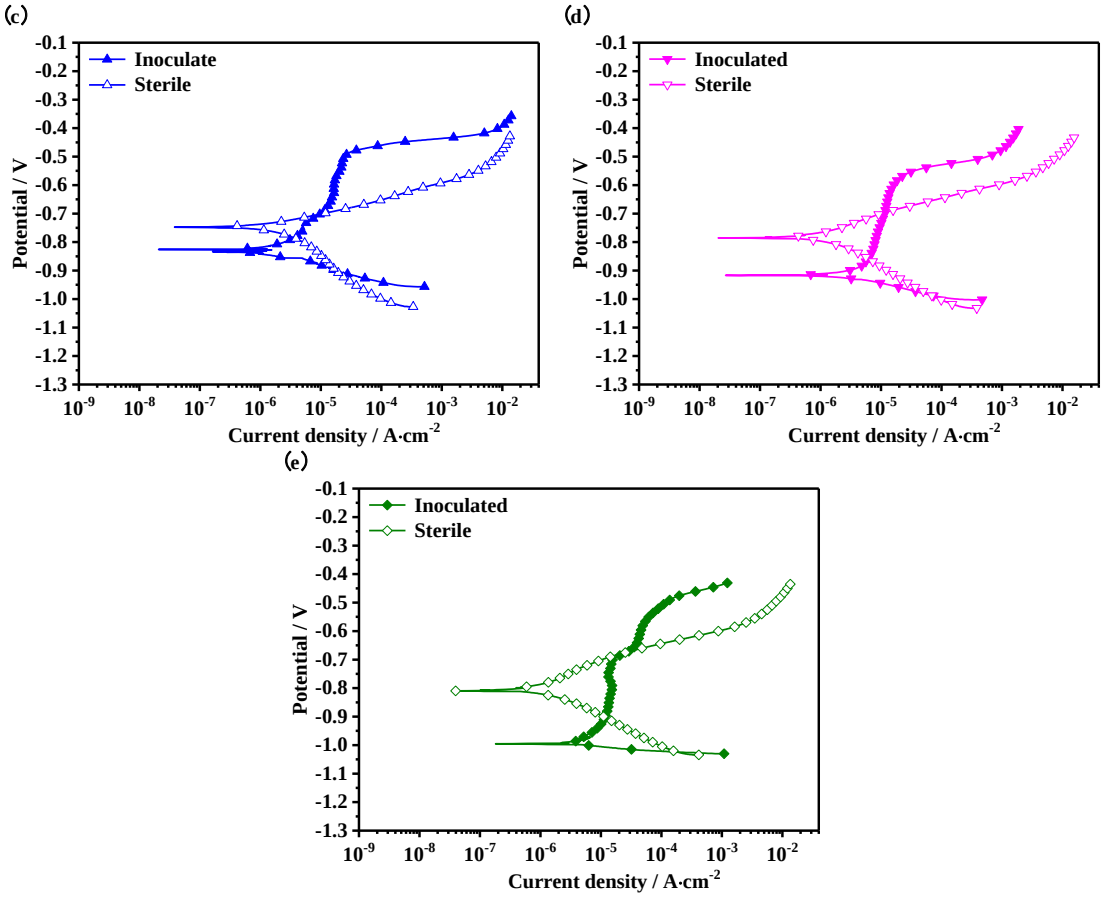

Figure 6. Polarization curves of L360N steel in the sterile and inoculated FBW (a) 1d, (b) 3d, (c) 7d, (d)14d, (e) 21d. Polarization measurements from -300.0 mV vs OCP to 300.0 mV vs OCP, with the scanning rate of 0.5 mV/s

In two different FBWs, the corrosion current density of the coupons treated with SRB is approximately 7.8 times higher than that of the sterile one. It can also be seen from the fitting data that the corrosion current density of the inoculated FBW is greater than that of the sterilized FBW on the 3rd, 7th and 14th day. The results show that SRB can accelerate the corrosion of L360N steel in the simulated FBW, which supports the EIS results.

Table 3. The corrosion parameters from the Tafel curves of L360N coupons for 1 d, 3 d, 7 d, 14 d and 21 d respectively in the sterile and inoculated FBW

Time /day	E_{corr} /mV		i_{corr} /μA·cm^{-2}		β_a /mV·dec^{-1}		β_c /mV·dec^{-1}	
	sterile	inoculated	sterile	inoculated	sterile	inoculated	sterile	inoculated
1	-0.740	-0.901	15.7	1.61	60.07	414.7	639.0	62.8
3	-0.743	-0.828	3.49	3.69	63.3	703.6	189.9	51.4
7	-0.748	-0.826	2.34	5.79	71.4	484.1	158.3	26.2
14	-0.785	-0.917	1.29	5.92	95.1	611.5	106.8	61.3
21	-0.809	-0.995	0.944	7.37	102.2	736.5	81.2	28.4

3.6 Micro characterization of the coupons surface

Figure 7 shows the Raman spectra of the corrosion products of L360N steel immersed in sterile and inoculated FBW for 21 days. Raman peaks appeared near 690 cm^{-1}, indicating that Fe_3O_4 was produced in both environments. Fe_3O_4 is an electric conductor with excellent density and stability, which can participate in the reduction reaction. In the inoculated FBW, the Raman peaks appeared at 209 and 271 cm^{-1}, and 209 cm^{-1} corresponds to FeS characteristic spectral line, belonging to the lattice mode. The spectral peak at 271 cm^{-1} is a structural disorder peak, which belongs to the asymmetric stretching vibration model of Fe-S bond in amorphous ferrous sulfide microcrystals [43].

The XPS results of corrosion products of the sterile and inoculated coupons immersed in FBW for 21 days are shown in Figure 8. The XPS results show that the corrosion products include Fe_2O_3, Fe_3O_4, Fe_2CO_3 and FeS. The fitting results in Table 4 indicate that there are significant differences among the substance contents of the corrosion products under different conditions. The content of Fe_2O_3 in the corrosion products is higher in the sterile FBW than that in the inoculated FBW. There is no iron sulfides in the sterile FBW, but the content of FeS in the corrosion products of the inoculated FBW is up to 25%. This is because the HS^- produced by the reduction of sulfate anions usually interacts with the ferrous iron produced by the anodic reaction to produce FeS [44].

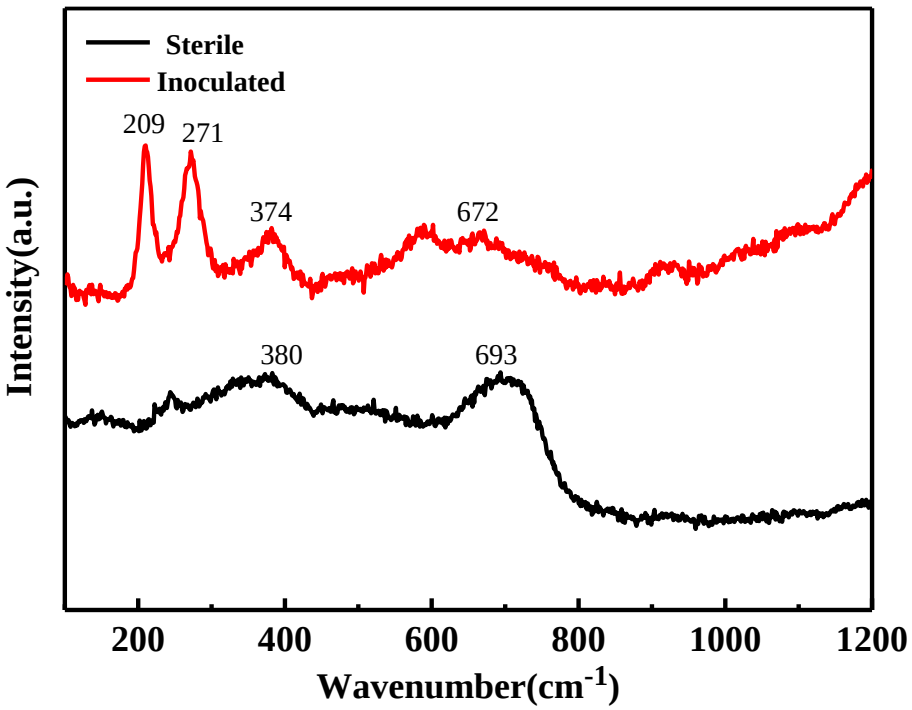

Figure 7. Raman spectra of the corrosion production of L360N steel after 21 d exposed in the sterile and inoculated FBW.(693 cm^{-1}: Fe_3O_4; 271 cm^{-1}: FeS; 209 cm^{-1}: FeS)

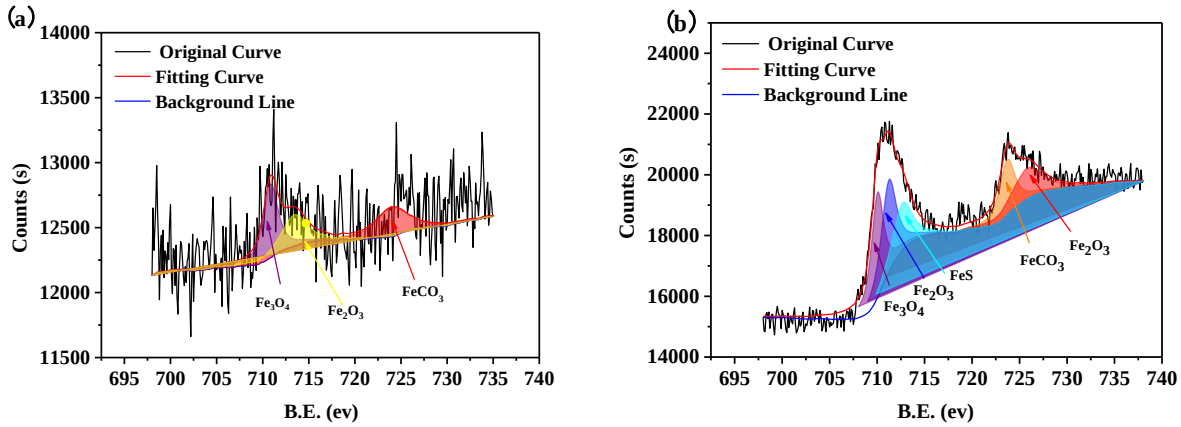

Figure 8. High-resolution XPS spectra of Fe 2p with an Al Kα (1486.6 eV) X-ray source at 15 kV, 150 W and a pass energy of 30 eV for a high-resolution scan after 21d exposed in the (a) sterile FBW and (b) inoculated FBW

Table 4. Results of EDS in the different positions on the surface of L360N steel in the sterile and inoculated FBW after 21 days (wt%)

Condition	Percentage(%)			
	Fe_2O_3	Fe_3O_4	FeS	$FeCO_3$
sterile	46.8	29.2	-	24.0
inoculated	32.4	20.2	26.8	20.6

Figure 9 shows the SEM cross-sectional morphology of L360N steel coupons under two conditions. As shown in Figure 9 (a), a very thin corrosion product layer appears on the coupon surface in the sterile FBW. The thickness of the corrosion product layer was further increased significantly in the inoculated FBW, as shown in Figure 9 (b), some cracks and holes appeared in the corrosion products. It can be seen from Figure 9 (b) that the corrosion products in the biofilm were entangled with EPS, and the loose white corrosion product film extended from the surface to the bottom of the film, indicating that the biofilm had an adsorption effect on the product Fe^{2+}. The FeS in the biofilm increased the roughness of the steel surface, which was conducive to SRB adhesion. The above results show that SRB affects the corrosion products formed on the surface of L360N steel.

After 21 days of exposure of L360N steel in sterile and inoculated FBW, the SEM morphologies of the corrosion products in different solutions are shown in Figure 10 and Figure 11. The corresponding EDS analysis results are show in Table 4.

The EDS results showed that the corrosion products contained C, O, Cl, S and Fe elements under both conditions. The C content of inoculated FBW was about 2 times higher than that of sterile FBW, which was mainly due to the adsorption of SRB metabolites and EPS on the surface of the coupon. And it can be observed from EDS that there was no S element on the surface of the coupon in the sterile FBW, while the S content in the inoculated FBW reached 14.86%.

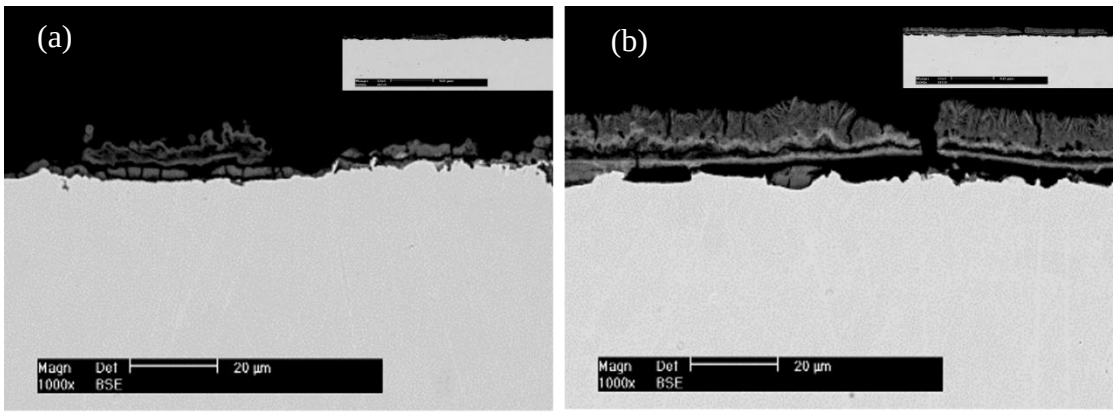

Figure 9. Cross-sectional microscopic appearance of L360N steel in simulated FBW after 21 days: (a) sterile, (b) inoculated

In the sterile FBW, loose corrosion products and particles of different sizes were observed on the coupon surface. The surface of deposit covered electrode was covered by integrated corrosion product film and some small crystals, as shown in Figure 10a. After the corrosion products were removed (Figure 11a.), the surface of the L360N steel substrate was corroded, and some shallow pits were observed. However, some scratches formed during the grinding process still existed, indicating that the corrosion of L360N in the sterile FBW was relatively slight.

In the inoculated FBW, the thickness of the corrosion products layer was further increased significantly, as shown in Figure 10b. Continuous biofilms with SRB, EPS and corrosion products can be seen, which were adsorbed in clusters on the surface of the coupon. The formation and structural changes of biofilm on the surface of coupons led to uneven electrochemical properties of the coupon surface, which created conditions for the occurrence of localized corrosion [45]. After the corrosion products were removed (Figure 11b.), as for the inoculated FBW, the corrosion surface was rougher than that of sterile FBW, and many small pits could be observed on the corrosion surface. The results indicated that the corrosion in the inoculated FBW was localized corrosion.

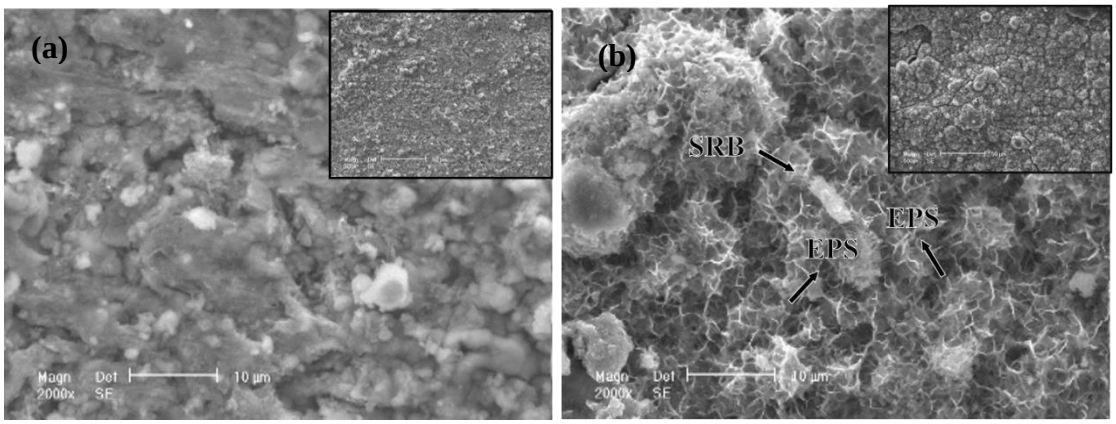

Figure 10. Microscopic appearance of the surface of L360N steel in simulated FBW after 21 days using a SEM (XL30-FEG, Holland) with energy dispersive X-ray analysis (EDS) at a 20 kV accelerating voltage :(a) sterile, (b) inoculated

Table 5. Results of EDS in the different positions on the surface of L360N steel in the sterile and inoculated FBW after 21 days (at%)

Condition	Percentage(%)				
	C	O	Cl	S	Fe
sterile	3.79	10.10	4.19	-	81.92
inoculated	7.83	11.17	2.11	14.86	64.03

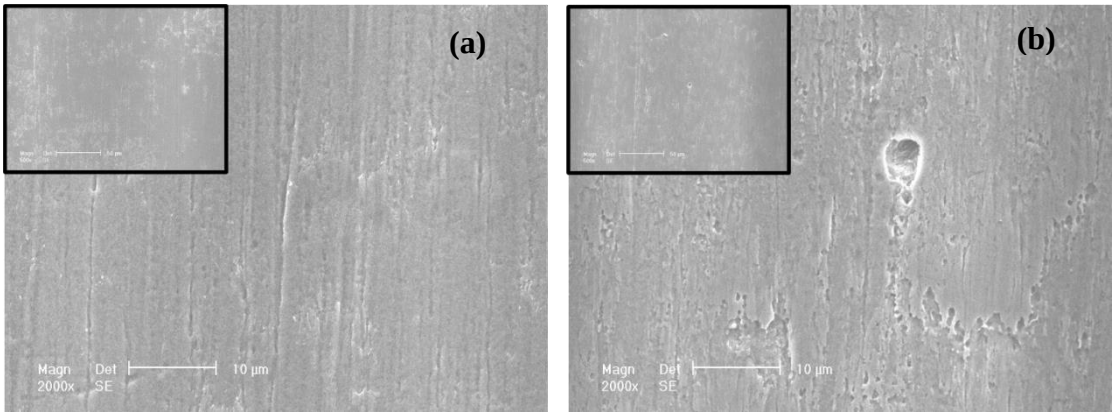

Figure 11. Microscopic appearance of surface of L360N steel in simulated FBW after removal of corrosion products: (a) sterile, (b) inoculated

After removing the corrosion products, CLSM was used to measure the pitting corrosion on the surface of L360N steel coupons. The three-dimensional pitting morphologies and maximum pitting depth curves are shown in Figure 12. For the coupon of sterile FBW, there are almost no corrosion pits in the three-dimensional pitting topography (Figure 12 (a)). In the SRB-inoculated FBW, several small corrosion pits with a maximum pitting depth of 2.5 μm can be observed in Figure 12(b), which is consistent with the SEM pitting image.

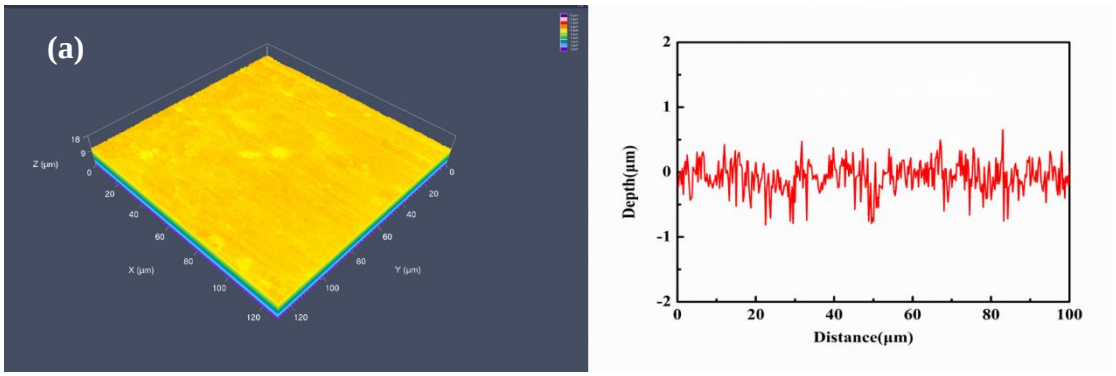

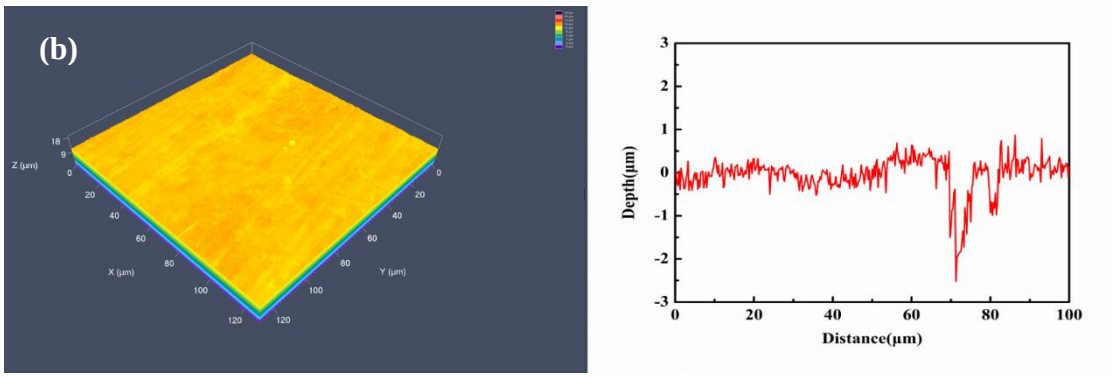

Figure 12. CLSM images of L360N steel after the removal of the corrosion products in FBW after 21 days: (a) sterile, (b) inoculated

3.7 Corrosion mechanism Discussion

3.7.1 The formation process of the corrosion products

The corrosion of L360N steel is an electrochemical reaction process, which consists of a series of anodic and cathodic reactions. In the simulated FBW inoculated with SRB, the initial corrosion is mainly CO_2 corrosion of L360N steel, which is manifested from the following reactions [46]:

Cathodic reaction:

$$2H_2CO_3 + 2e^- \rightarrow 2HCO_3^- \quad (2)$$

$$2HCO_3^- \rightleftharpoons {CO_3}^{2-} + 2H^+ + 2e^- \quad (3)$$

Anodic reaction:

$$Fe \rightarrow Fe^{2+} + 2e^- \quad (4)$$

$$Fe^{2+} + {CO_3}^{2-} \rightarrow FeCO_3 \quad (5)$$

$$Fe^{2+} + 2HCO_3^- \rightarrow 2Fe(HCO_3)_2 \quad (6)$$

$$2Fe(HCO_3)_2 \rightarrow FeCO_3 + CO_2 + H_2O \quad (7)$$

As shown in Figure 5(b), $FeCO_3$ was deposited on the surface of the steel coupon at the initial stage of corrosion. And OH^- can also react with Fe^{2+} to form $Fe(OH)_2$, because $Fe(OH)_2$ is extremely unstable, and ultimately can be converted to Fe_2O_3 and Fe_3O_4 [47]. Sulfate is regarded as an electron acceptor of organic alienation by SRB. During the exponential growth period of SRB, it could reduce SO_4^{2-} to S^{2-} [48]. The reactions of the iron in the simulated FBW inoculated with SRB are as follows [49]:

$$Fe + SO_4^{2-} + 9H^+ \rightarrow 4Fe^{2+} + HS^- + 4H_2O \quad (8)$$

Later, HS^- reacts with Fe^{2+} in the solution to produce FeS, which is adsorbed on the metal surface, as shown in the following reaction [50, 51]:

$$Fe^{2+} + HS^- \rightarrow FeS + H^+ \quad (9)$$

SRB colonies attached to the surface connect with each other to form a biofilm on the metal surface. The porous and loose biofilm are wrapped by SRB and FeS, thus improving the conductivity of the surface of the steel coupons. As shown in Figure 8 and Table 4, the XPS results suggested that the corrosion products under the two conditions were composed of Fe_2O_3, Fe_3O_4 and $FeCO_3$ in the simulated

FBW. The difference was that the content of FeS for the inoculated group reached 26.8%, and XPS was used to analyze the surface of coupon for 21 days under both conditions. The sterile group was mainly composed of sulfate, while the inoculation group was mainly composed of iron sulfide and sulfate, which to some extent showed that the activity of SRB led to the reduction of S chemical state. The sulfide adsorbed on the steel surface was similar to the corrosion of hydroxyl anion on iron, which affected the anodic process [17]. FeS was not an electron acceptor, but SRB led to extra cathodic regions on FeS film, allowing more SRB to harvest electrons [52]. As a result, a galvanic couple (anode) was formed between the sulfide (cathode) and the exposed steel, which promoted the corrosion of steel.

The promoting effect of SRB on corrosion is also related to H_2S in solution [53]. The dissolution of H_2S accelerates the rate of cathode reduction by increasing proton reduction [54]. Also, H_2S can dissociate and release H^+. The undissociated H_2S in the solution promotes the cathodic process by reacting directly with Fe^0. A large amount of H_2S are produced by metabolic activities of SRB in the biofilm, thereby reducing the local pH value of the biofilm [55].

$$H^+ + HS^- \rightleftharpoons H_2S \quad (10)$$

$$Fe^0 + H_2S \rightleftharpoons FeS + H_2 \quad (11)$$

3.7.2 Occurrence of pitting corrosion under the Biofilm

Biofilm is the main form of survival for SRB in natural environment. Under the physiological activity of SRB, biofilm are usually formed locally, causing galvanic corrosion on the metal surface , thereby causing localized corrosion [56, 57]. SRB can adsorb on the metal surface, reproduce and complete the entire metabolic process in the biofilm. The hydrolyzed biofilm produces hydrophilic polar groups, forming a hydrated iron oxide film with Fe^0 on the steel surface, and generating oxygen gradient in the biofilms at the bottom of the anoxic zone. This will cause pits under the biofilm. The biofilm is divided into a small anodic region (beneath the surface film) and a large peripheral cathode region, which produces electrons flowing to the cathode and an aggressive form of corrosion, resulting in pitting corrosion [47, 58].

A biofilm is mainly composed of microbial cells and EPS. EPS not only promotes the growth of SRB, but also affects the corrosion process of metals. EPS has changed the equilibrium state of the interface between the metal and the corrosive environment [57, 59]. Especially, the uniformity of $FeCO_3$ and FeS in the corrosion product layer is changed under the action of biofilm, which increases the galvanic corrosion [60]. Therefore, the above factors constitute the main reason for pitting corrosion under the biofilm. As shown in Figure 11(a) and Figure 12(a), the steel surface in the sterile FBW only experiences uniform corrosion, and the pitting corrosion severity caused by SRB is shown in Figure 11(b) and Figure 12(b).

The high-conductivity sulfide produced in the inoculated group can improve the dielectric properties of the corrosion product film and accelerate the anodic dissolution process under the biofilm [12]. During the LPR and EIS measurements on 7d, 14d and 21d, the negative displacement of R_p and R_{ct} values after SRB inoculation also indicates the decrease of the corrosion resistance of the coupons.

3.7.3 Synergistic effect of CO_2 and SRB on corrosion of L360N steel

The schematic diagram of the corrosion mechanism of L360N steel coupons in the simulated FBW with inoculated SRB is shown in Figure 13. At the initial stage of the experiment, as shown in Figure 13(a), CO_2 predates SRB in the process of metal corrosion. A relatively dense layer of corrosion products ($FeCO_3$) is formed on the metal surface. The formed $FeCO_3$ corrosion product film will hinder the penetration of cations. After that, the anions in the solution can pass through the corrosion product film without any resistance, and further react with the steel substrate. SRB begins to adsorb on the steel surface and then grow, proliferate and participate in the corrosion process during the exponential growth period. Then SRB forms biofilm and metabolites (FeS) on the surface of $FeCO_3$ corrosion product layer, as shown in Figure 13(b). Due to the inhomogeneity of the biofilm and the electrical activity of FeS, a large number of SRB continuously adsorb on the surface, as shown in Figure 13(c), which makes SRB in the FBW containing CO_2 accelerate the cathodic depolarization reaction [61].

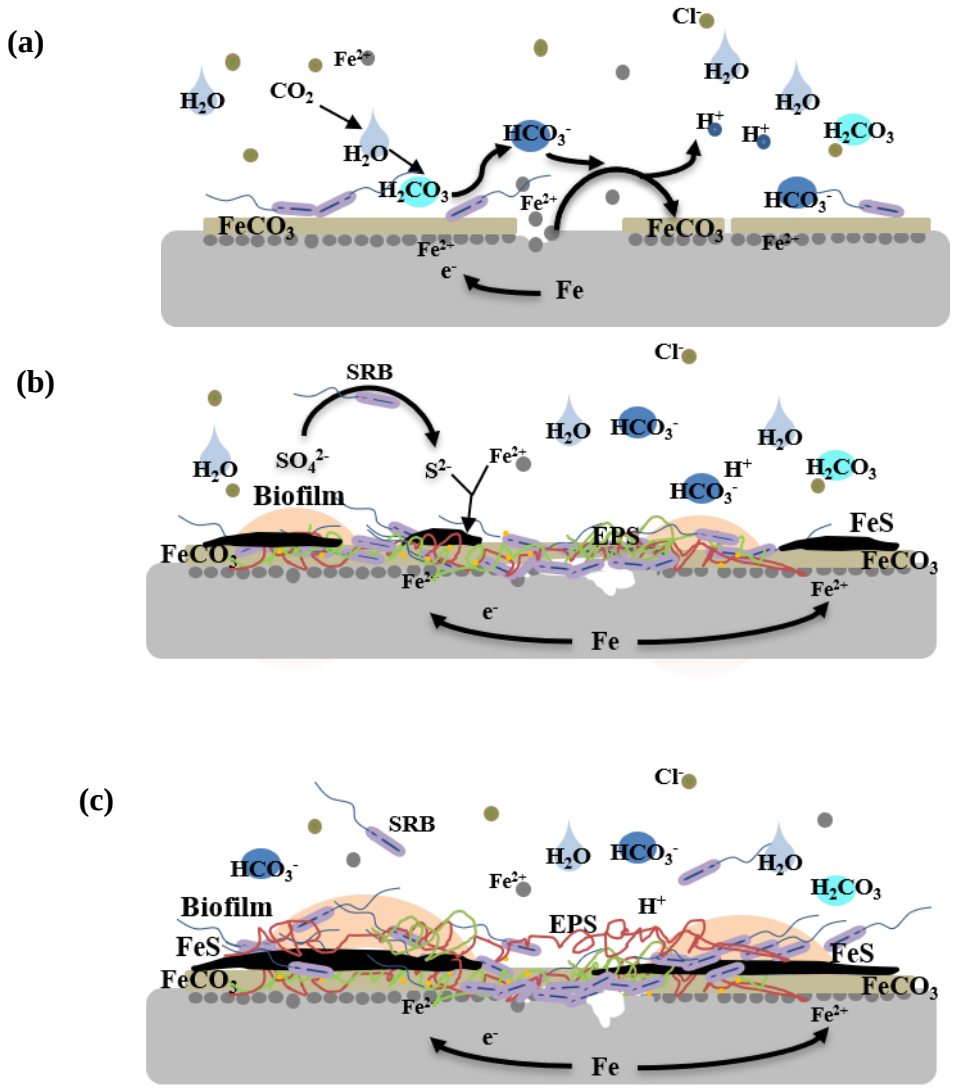

Figure 13. Schematic diagram of corrosion process and biofilm formation in SRB inoculated FBW (a). initial stage, (b)middle stage, (c) final stage

4. CONCLUSION

In this paper, the corrosion mechanism of L360N steel in the FBW containing SRB was studied by electrochemical tests and surface characterization. The conclusions can be summarized as follows:

(1) FBW containing SRB accelerates corrosion of L360N steel. The weight loss data indicated that the corrosion rate of FBW containing SRB was 5 times higher than that of sterile group.

(2) In the inoculated FBW, the corrosion of CO_2 on metals is prior to that of SRB on L360N. Under the synergistic effect of SRB metabolites and CO_2, the anodic dissolution of the material was promoted, and the corrosion under this condition was mainly pitting corrosion.

(3) The corrosion product layer formed by biofilm, EPS, ferrous sulfide, and $FeCO_3$ changed the phase interface between the metal and the corrosive medium, and the inhomogeneity of the corrosion product layer promoted the occurrence of local corrosion.

DISCLOSURE STATEMENT
No potential conflict of interest was reported by the author(s).

ACKNOWLEDGEMENT
This work was supported by the Research Institute of Natural Cas Technology, China.

DATA AVAILABILITY STATEMENT
Some or all data, models, or codes that support the findings of this study are available from the corresponding author upon reasonable request.

References

1. H. K. Nie, Q. Chen, G. G. Zhang, C. X. Sun, P. W. Wang and Z. Y. Lu, *Nat. Gas Ind. B*., 8 (2021) 217.
2. G. Y. Wu, W. W. Zhao, Y. R. Wang, Y. F. Tang and M. Xie, *Eng. Fail. Anal.*, 130 (2021) 105796.
3. X. H. Ma and J. Xie, *Pet. Explor. Dev*, 45 (2018) 172.
4. S. K. Gao, D. Z. Dong, K. Tao, W. Guo, X. J. Li and S. R. Zhang, *J. Nat. Gas Sci. Eng.*, 85 (2021) 103648.
5. A. Abramowska, D. K. Gajda,K. Kiegiel, A. Mis´kiewicz, P. Drzewicz and G. Zakrzewska-Kołtuniewicz, *Sep. Sci. Technol.*, 53 (2017) 1207.
6. A. Shaikh, C. L. Dai, Y. P. Sun, Q. You, A. S. Qureshi, G. Zhao, V. Foutou, A. Bakhsh, N. Khan, Z. Abro and M. W. Zhao, *J. Petrol. Sci. Eng.*, 208 (2022) 109674.
7. D. Zhukov, S. Konovalov and A. Afanasyev, *Eng. Fail. Anal.*, 109 (2020) 104359.
8. M. Yue and Y. C. Wang, *Drill. Prod. Technol.,* 41 (2018) 125.
9. R. Melchers. *Corros. Mater.*, 37 (2012) 11.
10. R. J. Xiao, G. Q. Xiao, B. Huang, J. H. Feng and Q. H. Wang, *Eng. Fail. Anal*, 68 (2016) 113.
11. H. W. Liu, C. Y. Fu, T. Y. Gu, G. A. Zhang, Y. L. Lv, H. T. Wang and H. F. Liu, *Corr. Sci.*, 100 (2015) 484.
12. S. Q. Feng, Y. C. Li, H. M. Liu, Q. P. Liu, X. Chen, H. B. Yu and C. F. Chen, *J. Nat. Gas Sci. Eng.*, 80 (2020) 103395.
13. B. J. Little, D. J. Blackwood, J. Hinks, F. M. Lauro, E. Marsili, A. Okamoto, S. A. Rice, S. A. Wade and H. C. Flemming, *Corr. Sci.*, 170 (2020) 108641.
14. S. N. Victoria, A. Sharma and R. Manivannan, *J. Indian. Chem. Soc.*, 98 (2021) 100083.

15. X. Jiang, Q. Zhang, D. R. Qu, K. Xu and X. L. Song, *J. Nat. Gas Sci. Eng.*, 82 (2020) 103492.
16. H. X. Wan, D. D. Song, D. W. Zhang, C. W. Du, D. K. Xu, Z. Y. Liu, D. Ding and X. G. Li, *Bioelectrochemistry*, 121 (2018) 18.
17. T. Q. Wu, M. C. Yan, L. B. Yu, H. T. Zhao, C. Sun, F. C. Yin and W. Ke, *Corr. Sci.*, 157 (2019) 518.
18. J. Xu, Y. L. Bai, T. Q. Wu, M. C. Yan, C. K. Yu and C. Sun, *Eng. Fail. Anal*, 100 (2019) 192.
19. I. B. Beech and C. C. Gaylarde, *Braz. J. Microbiol*., 30 (1999) 117.
20. T. Q. Wu, M. C. Yan, D. C. Zeng, J. Xu, C. K. Yu, C. Sun and W. Ke, *Acta. Metall. Sin-engl.*, 28 (2015) 93.
21. E. S. Bastin, B. Anderson, F. E. Greer, C. A. Merreet and G. Moulton, *AAPG. BULL.*, 12 (1926) 1270.
22. V. W. Kuhr and C. Ah, *Corrosion*, 17 (1961) 293.
23. R. L. Starkey. *Bacteriol. Rev*, 22 (1958) 154.
24. R. A. King and J. Miller, *Nature*, 233 (1971) 49.
25. P. I. Warren, *Nature*, 217 (1968) 1265.
26. D. H. Pope and E. A. Morris, *Mater. Perform.*, 34 (1995) 23.
27. I. P. Pankhania, A. N. Mossavi and W. A. Hamilton, *Microbiology*, 132 (1986) 3357.
28. D. K. Xu, Y. C. Li and T. Y. Gu, *Bioelectrochemistry*, 110 (2016) 52.
29. R. Jia, J. L. Tan, P. Jin, D. J. Blackwood, D. K. Xu and T. Y. Gu, *Corr. Sci.*, 130 (2018) 1.
30. M. C. Yan, C. Sun, J. Xu, J. H. Dong and W. Ke, *Corr. Sci.*, 80 (2014) 309.
31. E. Dennis and G. Julia, *Appl. Environ. Microbiol.*, 80 (2014) 1226.
32. I. B. Beech and W. S. Cheung, *Int. Biodeter. Biodegr*., 35 (1995) 59.
33. R. Javaherdashti, *Anti-Corros Method M*., 46 (1999) 173.
34. H. X. Wan, D. D. Song, D. W. Zhang, C. W. Du, D. K. Xu, Z. Y. Liu, D. Ding and X. G. Li, *Bioelectrochemistry*, 121 (2018) 18.
35. Z. Li, H. X. Wan, D. D. Song, X. D. Liu, Z. Y. Li and C. W. Du, *Bioelectrochemistry*, 126 (2019) 121.
36. H. W. Liu, T. Y. Gu, M. Asif, G. A. Zhang and H. F. Liu, *Corr. Sci.*, 114 (2017) 102.
37. H. W. Liu, T. Y. Gu, G. A. Zhang, Y. F. Cheng, H. T. Wang and H. F. Liu, *Corr. Sci.*, 102 (2016) 93.
38. H. W. Liu, T. Y. Gu, G. A. Zhang, H. F. Liu and Y. F. Cheng, *Corr. Sci.*, 136 (2018) 47.
39. F. Xie, Z. W. Guo, D. Wang, R. Lie, M. Wu, Y. Zong and Y. C. Wang, *Int. J. Electrochem. Sci*., 14 (2019) 2693.
40. B. X. Wei, J. Xu, Q. Fu, Q. Y. Qin, Y. L. Bai, C. Sun, C. Wang, Z. Y. Wang and W. Ke, *J. Mater. Sci. Technol.*, 87 (2021) 1.
41. J. Xu, R. Jia, D. Q. Yang, C. Sun and T. Y. Gu, *J. Mater. Sci. Technol.*, 35 (2019) 109.
42. T. Q. Wu, M. C. Yan, D. C. Zeng, J. Xu, C. K. Yu, C. Sun and W. Ke, *Acta Metall Sin-engl*, 28 (2014) 93.
43. B. W. A. Sherar, I. M. Power, P. G. Keech, S. Mitlin, G. Southam and D.W. Shoesmith, *Corr. Sci.*, 53 (2011) 955.
44. T. Siddharth, P. Sridhar, V. Vinila and R. D. Tyagi, *J. Environ. Manage.*, 287 (2021) 112307.
45. T. Y. Gu, R. Jia, T. Unsal and D. K. Xu, *J. Mater. Sci. Technol.*, 35 (2019) 631.
46. G. A. Zhang and Y. F. Cheng, *Corr. Sci.*, 51 (2009) 87.
47. B. Grambow, C. Martin, A. Abdelouas, G. Karakurt, H. El Hajj and Y. El Mendili, *Corr. Sci.*, 76 (2013), 432.
48. D. X. Sun, M. Wu and F. Xie, *Mater. Sci. Eng. A*, 721 (2018) 135.
49. J. Xu, K. X. Wang, C. Sun, F. H. Wang, X. M. Li, J. X. Yang and C. K. Yu, *Corr. Sci.*, 53 (2011) 1554.
50. M. Stipaničev, F. Turcu, L. Esnault, E. W. Schweitzer, R. Kilian and R. Basseguy, *Electrochim. Acta*, 113 (2013) 390.
51. Q. Y. Qin, J. Xu, B. X. Wei, Q. Fu, L. Q. Gao, C. K. Yu, C. Sun and Z. Y. Wang,

Bioelectrochemistry, 142 (2021) 107911.
52. R. Jia, D. Q. Yang, D. K. Xu and T. Y. Gu, *Bioelectrochemistry*, 118 (2017) 38.
53. F. Q. Fan, B. Y. Zhang, J. B. Liu, Q. H. Cai, W. Y. Lin and B. Chen, *Chemosphere*, 238 (2020) 124655.
54. R. G. Esquivel, G. Z. Olivares, M. J. H. Gayosso and A. G. Trejo, *Mater. Corros.*, 62 (2011) 61.
55. Z. H. Dong, W. Shi, H. M. Ruan and G. A. Zhang, *Corr. Sci.*, 53 (2011) 2978.
56. F. M. Alabbas, C. Williamson, S. M. Bhola, J. R. Spear, D. L. Olson, B. Mishra and A. E. Kakpovbia, *Int. Biodeter. Biodegr.*, 78 (2013) 34.
57. T. Liu and Y. F. Cheng, *J. Alloy. Compd.*, 729 (2017) 180.
58. S. Q. Chen and D. Zhang, *Corr. Sci.*, 136 (2018) 275.
59. X. Q. Song, Y. X. Yang, D. L. Yu, G. H. Lan, Z. L. Wang and X. J. Mou, *J. Pet. Sci. Eng.*, 146 (2016) 803.
60. T. Q. Wu, C. Yan, D. C. Zeng, J. Xu, C. Sun, C. K. Yu and W. Ke, *Corr. Sci.*, 91 (2015) 86
61. U. Eduok and E. Ohaeri, J. Szpunar, *Mat. Sci. Eng. C-Mater.*, 105 (2019) 110095.